PARAMETER CALIBRATION OF THE BONDING MODEL FOR ASTRAGALUS ROOT BASED ON DISCRETE ELEMENTS

/

基于离散元的黄芪根 BONDING 模型参数标定

Jun YOU, Xin DU *), Qi-xin SUN, Shu-fa CHEN, Jing-yi MAO [1]
Jiangsu Ocean University, Lianyungang 222005/China
Tel: 0086-0518-85895322; E-mail: xindu @jou.edu.cn
Corresponding author: Xin Du
DOI: https://doi.org/10.35633/inmateh-79-37

***Keywords:** Astragalus Membranaceus Root; Bonding Model; Placket-Burman; Steepest ascent; Box-Behnken; Discrete Element Method*

ABSTRACT

To address the issue of uneven fracture during the processing of Astragalus slices, this study first establishes a discrete element Bonding model for Astragalus roots, filling the gap in the calibration of its bonding parameters. Through uniaxial compression tests and multiple optimization experiments, the optimal parameters were determined, with simulation errors below 1.6% and validation errors for the fracture rate ≤ 12.7%, providing theoretical support for the development of processing equipment for Astragalus slices.

摘要

针对黄芪饮片加工断裂不均问题，本研究首次建立黄芪根离散元 Bonding 模型，填补其黏结参数标定空白。经单轴压缩试验与多组优化试验确定最优参数，仿真误差低于 1.6%，破碎率验证误差≤12.7%，可为黄芪饮片加工设备研发提供理论支撑。

INTRODUCTION

Astragalus membranaceus is a valuable traditional Chinese medicinal herb that functions in invigorating qi and enhancing body immunity. Its dried root has a long medicinal history and was incorporated into the medicine-food homologous catalogue in 2023, reflecting its significant medicinal value and industrial prospects (*Xi et al., 2023; Ji et al., 1998*). With the development of the modern Astragalus industry, promoting the mechanization and precision of processing operations such as root slicing and crushing has become essential. However, owing to the complex internal fibrous structure and unique mechanical properties of Astragalus root, uneven fractures and excessive powder production often occur during processing, which severely reduce the quality of prepared slices and production efficiency (*Duan, 2005*). The Discrete Element Method (DEM) coupled with the Bonding Model provides an effective means to simulate the bonding and fracture behaviors of granular materials and accurately reflect their mechanical responses, which has been widely applied in agricultural engineering (*Zhao et al., 2021; Zeng et al., 2021*). Nevertheless, existing DEM studies on Astragalus root lack accurate calibration of key Bonding Model parameters, including cohesion and elastic modulus, which limits the simulation accuracy of mechanical property evolution and fracture behaviors during processing. Therefore, calibrating these bonding parameters and establishing a high-precision DEM model is of great theoretical and practical importance for revealing tool-material interaction mechanisms, optimizing equipment design, and improving slice quality and active ingredient retention. Since DEM was proposed for soil mechanics by *Cundall et al.* (*1979*), it has been widely used in granular material operations such as mixing, conveying, filling and crushing (*Lu et al., 2015; Shen et al., 2016*). The Bonded Particle Model proposed by *Potyondy et al.* (*2004*) realizes fracture simulation via inter-particle bonding and has been widely adopted in agricultural research. Previous studies have completed bonding parameter calibration for various agricultural materials (e.g., coated fertilizer, garlic cloves, crop stems, corn ears) via mechanical tests such as uniaxial compression (*Du et al., 2022; Li et al., 2025; Xu et al., 2024; Gao et al., 2024; Xie et al., 2023; Li et al., 2025*). Relevant calibrations have also been conducted for banana stalks, walnuts and cotton seeds (*Zhang et al., 2023; Zhou et al., 2023; Hu et al., 2022*), and the model has been applied to analyze fracture mechanisms in Cyperus esculentus harvesting (*Zhu et al., 2022*).

---

[1] *Jun You, MA. Eng Stud.; Xin Du*, Lecturer Ph.D. Eng; Qixin Sun, Prof. Ph.D. Eng; Shufa Chen, Prof. Ph.D. Eng; Jingyi Mao, B.S Stud.*

These studies have promoted the application of the Bonding Model and parameter calibration in agricultural material processing. Building on existing research (*Du et al., 2022; Li et al., 2023; Xu et al., 2024; Gao et al., 2024; Xie et al., 2023; Li et al., 2025*), this study focuses on Astragalus root. Using the ultimate crushing load and displacement obtained from uniaxial compression tests, the Bonding Model parameters are optimized by combining the Plackett-Burman test, the Steepest Ascent test and the Box-Behnken test. The reliability of the calibrated parameters is verified through comparative tests between physical experiments and simulations.

This study aims to provide accurate basic parameters for DEM simulation of Astragalus processing equipment and support the intelligent development of related machinery. It fills the gap in DEM parameter calibration for Astragalus root and provides a new reference for mechanical simulation of granular traditional Chinese medicinal materials.

MATERIALS AND METHODS

Bonding Model

In discrete element numerical simulations, the bond-based contact model, designed by *Potyondy et al.* (*2004*), is a core method for studying material fracture. This model abstracts the interaction between particles as virtual connecting bonds, constructing a mechanical transmission network to simulate the fracture process. Although differing in theory and scale from the finite element method, it complements FEM in multi-physics field coupling. Bond elements possess multi-dimensional mechanical responses, undergoing tension, compression, torsion, and other deformations under load, following Hooke's law. The force-deformation relationship can be quantified using elastic moduli. When stress or torque exceeds a critical threshold, the bond breaks, simulating material crack propagation. The bonding contact model assumes that the bond between two particles is a virtual flat plate or cylinder, as illustrated in Figure 1.

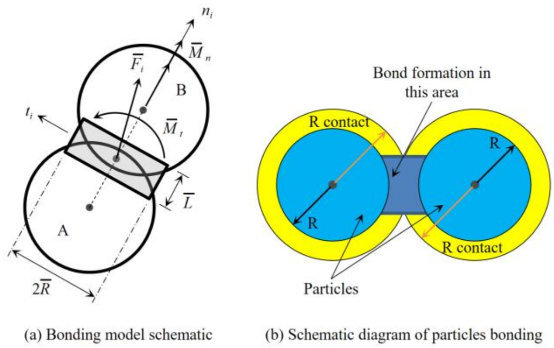

Fig. 1 - Schematic diagram of Bonding Model principle and particle bonding

During relative displacement between two particles, the plate or cylindrical structure is subjected to mechanical actions such as tension, bending, and shear. The force and moment increments on the bond are calculated as follows:

$$\begin{cases} \delta F_n = -v_n S_n A \delta t \\ \delta F_t = -v_t S_t A \delta t \\ \delta M_n = -\omega_n S_t J \delta t \\ \delta M_t = -\omega_t S_n \dfrac{J}{2} \delta t \end{cases} \tag{1}$$

$$\begin{cases} A = \pi R_B^2 \\ J = \dfrac{1}{2} \pi R_B^4 \end{cases} \tag{2}$$

where:

δF_n is the normal force, N; δF_t is the tangential force, N; v_n is the normal velocity, m/s; v_t is the tangential velocity, m/s; S_n is the normal stiffness, N/m; S_t is the tangential stiffness, N/m; δ_t is the simulation time step, s; A is the contact area between particles, m²; δM_n is the normal moment increment, N·m; δM_t is the tangential moment increment, N·m; ω_n is the normal angular velocity, rad/s; ω_t is the tangential angular velocity, rad/s; J is the particle moment of inertia, mm⁴; R_B is the bonded disk radius, mm.

Discrete Element Modeling of Astragalus Root Segment Particles

Astragalus roots from Dingxi, Gansu (density 0.912g/cm³) were cut into 37.5 mm-long uniform segments for geometric modeling. The Bonded Particle Method (BPM) (*Su et al., 2021*) was adopted to establish the discrete element model (DEM) for Astragalus root fracture analysis, where equal-diameter spherical particles are bonded to represent the root structure. A cylindrical bonding model was constructed, and 0.5 mm-radius spherical particles were finally selected for parameter calibration after comprehensive comparison of different particle sizes.

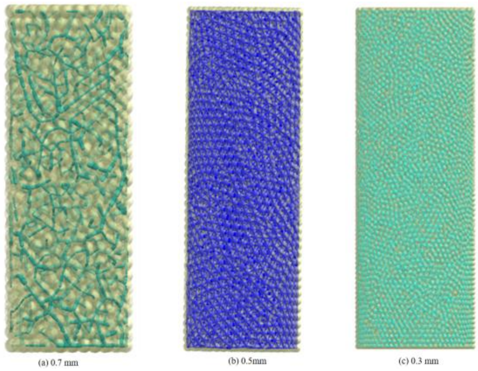

Fig. 2 - Filling diagrams using spherical particles of different diameters

Uniaxial Compression Test

Physical Experiment

Astragalus root segments with a diameter of 14 mm and length of 37.5 mm were selected. Uniaxial compression tests were performed on the segments using a universal testing machine. Loading was applied at a constant speed of 0.1 mm/s until specimen failure occurred. The loading process of a specimen during the uniaxial compression test is shown in Figure 3. The test was repeated 8 times, and the average displacement-load curve for the Astragalus segments is presented in Figure 4.

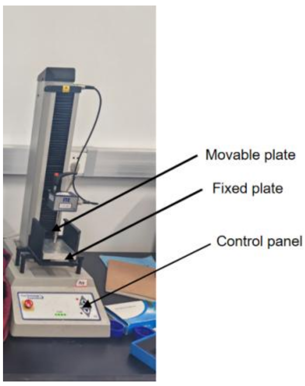

Fig. 3 - Universal testing machine

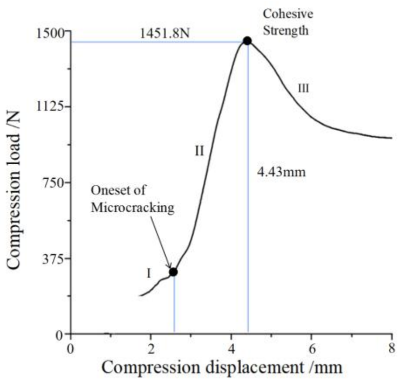

Fig. 4 - Displacement-load curve

Simulation Experiment

A uniaxial compression simulation model consistent with physical tests was established in EDEM 2022 (Figure 5). Material parameters are listed in Table 1. Simulation settings: total time 4 s, time step 8.5×10^{-6} s, data interval 0.01 s, grid size 3 times the radius of the smallest spherical particle.

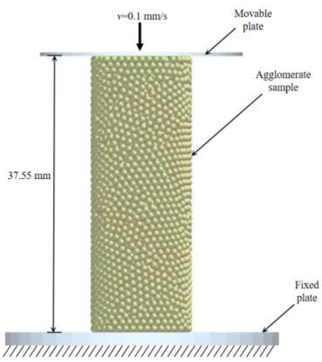

Fig. 5 - Uniaxial compression experiment simulation setup

Table 1

Physical property parameters of materials

Item	Parameter	Value
Astragalus	Poisson's Ratio	0.25
	Density (kg/m³)	912
	Shear Modulus (Pa)	2.17×10^{6}
Steel	Poisson's Ratio	0.3
	Density (kg/m³)	7850
	Shear Modulus (Pa)	8×10^{9}
Astragalus-Steel	Coefficient of Restitution	0.45
	Static Friction Coefficient	0.22
	Rolling Friction Coefficient	0.10
Astragalus-Astragalus	Coefficient of Restitution	0.51
	Static Friction Coefficient	0.43
	Rolling Friction Coefficient	0.15

Plackett-Burman Experimental Design

The Plackett-Burman design assesses factor significance by comparing two-level responses for each factor, taking ultimate crushing load (F_R) and displacement (L) as optimization objectives. Five factors (normal stiffness A, tangential stiffness B, critical normal stress C, critical tangential stress D, bonding radius E) were set at two levels. An 11-run design with 6 dummy terms for error analysis was used, and detailed factor levels are given in Table 2.

Table 2

Plackett-Burman experimental factor levels

No.	A	B	C	D	E
1	1.0×10^{7}	8.0×10^{6}	6.1×10^{6}	4.7×10^{6}	0.55
2	1.1×10^{7}	9.0×10^{6}	7.3×10^{6}	5.8×10^{6}	0.60

The simulation experimental design results are shown in Table 3.

Table 3

Plackett-Burman experimental design

No.	A	B	C	D	E	F_R/(N)	L/(mm)
1	1.1×10^{7}	9.0×10^{6}	6.1×10^{6}	5.8×10^{6}	0.60	1511	4.85
2	1.0×10^{7}	9.0×10^{6}	7.3×10^{6}	4.7×10^{6}	0.60	1484	5.05
3	1.1×10^{7}	8.0×10^{6}	7.3×10^{6}	5.8×10^{6}	0.55	1252	4.41
4	1.0×10^{7}	9.0×10^{6}	6.1×10^{6}	5.8×10^{6}	0.60	1480	5.15
5	1.0×10^{7}	8.0×10^{6}	7.3×10^{6}	4.7×10^{6}	0.60	1398	4.65
6	1.0×10^{7}	8.0×10^{6}	6.1×10^{6}	5.8×10^{6}	0.55	1207	4.49
7	1.1×10^{7}	8.0×10^{6}	6.1×10^{6}	4.7×10^{6}	0.60	1421	4.15
8	1.1×10^{7}	9.0×10^{6}	6.1×10^{6}	4.7×10^{6}	0.55	1315	3.95
9	1.1×10^{7}	9.0×10^{6}	7.3×10^{6}	4.7×10^{6}	0.55	1311	4.25
10	1.0×10^{7}	9.0×10^{6}	7.3×10^{6}	5.8×10^{6}	0.55	1278	4.72
11	1.1×10^{7}	8.0×10^{6}	7.3×10^{6}	5.8×10^{6}	0.60	1419	4.39
12	1.0×10^{7}	8.0×10^{6}	6.1×10^{6}	4.7×10^{6}	0.55	1207	4.45

Steepest Ascent Experimental Design

The Plackett-Burman results indicated that factor C had no significant effect on the experimental outcomes; therefore, C was fixed at 6.7×10^{6} Pa. A steepest ascent experiment was conducted to identify parameter combinations closer to the true values, with the experimental plan and results shown in Table 4.

Table 4

Steepest ascent experimental design

No.	A	B	D	E	F_R/(N)	L/(mm)
1	1.05×10^{7}	8.50×10^{6}	5.25×10^{6}	0.575	1357.9	4.20
2	9.65×10^{6}	8.63×10^{6}	5.80×10^{6}	0.585	1372.2	4.23
3	8.80×10^{6}	8.76×10^{6}	6.35×10^{6}	0.595	1401.1	4.28
4	7.95×10^{6}	8.89×10^{6}	6.90×10^{6}	0.605	1409.5	4.31
5	7.10×10^{6}	9.02×10^{6}	7.45×10^{6}	0.615	1430.9	4.35

No.	A	B	D	E	F_R/(N)	L/(mm)
6	6.25×10^6	9.15×10^6	8.00×10^6	0.625	1437.3	4.39
7	5.40×10^6	9.28×10^6	8.55×10^6	0.635	1458.1	4.41
8	4.55×10^6	9.41×10^6	9.10×10^6	0.645	1470.2	4.50

Box-Behnken Experimental Design

Design-Expert software was utilized to construct a Box-Behnken simulation experimental system for the significant contact parameters. The 7th level from the steepest ascent test was set as the central reference point (coded value 0). The 6th and 8th levels were defined as the low level (coded value -1) and high level (coded value +1), respectively, as shown in Table 5.

Table 5

Coding table for significant factor levels

Level	A	B	D	E
-1	6.25×10^6	9.15×10^6	8.00×10^6	0.625
0	5.40×10^6	9.28×10^6	8.55×10^6	0.635
+1	4.55×10^6	9.41×10^6	9.10×10^6	0.645

The experimental plan and results are shown in Table 6.

Table 6

Box-Behnken experimental design

No.	A	B	D	E	F_R/(N)	L/(mm)
1	4.55×10^6	9.15×10^6	8.55×10^6	0.635	1398.4	3.90
2	6.25×10^6	9.15×10^6	8.55×10^6	0.635	1449.7	4.34
3	4.55×10^6	9.41×10^6	8.55×10^6	0.635	1439.3	3.51
4	6.25×10^6	9.41×10^6	8.55×10^6	0.635	1501.0	5.25
5	5.40×10^6	9.28×10^6	8.00×10^6	0.625	1416.0	3.85
6	5.40×10^6	9.28×10^6	9.10×10^6	0.625	1415.6	4.05
7	5.40×10^6	9.28×10^6	8.00×10^6	0.645	1484.4	4.68
8	5.40×10^6	9.28×10^6	9.10×10^6	0.645	1485.0	4.78
9	4.55×10^6	9.28×10^6	8.55×10^6	0.625	1351.9	3.21
10	6.25×10^6	9.28×10^6	8.55×10^6	0.625	1453.3	4.35
11	4.55×10^6	9.28×10^6	8.55×10^6	0.645	1459.2	4.44
12	6.25×10^6	9.28×10^6	8.55×10^6	0.645	1522.7	5.08
13	5.40×10^6	9.15×10^6	8.00×10^6	0.635	1444.6	4.24
14	5.40×10^6	9.41×10^6	8.00×10^6	0.635	1475.0	4.36
15	5.40×10^6	9.15×10^6	9.10×10^6	0.635	1455.0	4.37
16	5.40×10^6	9.41×10^6	9.10×10^6	0.635	1474.9	4.35
17	4.55×10^6	9.28×10^6	8.00×10^6	0.635	1420.0	3.54
18	6.25×10^6	9.28×10^6	8.00×10^6	0.635	1501.7	4.57
19	4.55×10^6	9.28×10^6	9.10×10^6	0.635	1418.4	3.51
20	6.25×10^6	9.28×10^6	9.10×10^6	0.635	1502.0	4.56
21	5.40×10^6	9.15×10^6	8.55×10^6	0.625	1414.4	3.65
22	5.40×10^6	9.41×10^6	8.55×10^6	0.625	1430.3	3.95
23	5.40×10^6	9.15×10^6	8.55×10^6	0.645	1492.9	4.45
24	5.40×10^6	9.41×10^6	8.55×10^6	0.645	1510.6	5.40
25	5.40×10^6	9.28×10^6	8.55×10^6	0.635	1462.0	4.25
26	5.40×10^6	9.28×10^6	8.55×10^6	0.635	1452.0	4.45
27	5.40×10^6	9.28×10^6	8.55×10^6	0.635	1471.0	4.37
28	5.40×10^6	9.28×10^6	8.55×10^6	0.635	1447.0	4.51
29	5.40×10^6	9.28×10^6	8.55×10^6	0.635	1458.0	4.65

RESULTS AND ANALYSIS

Uniaxial Compression Test Results

As shown in Figure 4, the force-displacement curve of Astragalus root segments consists of three stages. Stage I involves local damage with rapid initial force growth followed by a slow increase, while the main body remains intact. Stage II is the main failure process: the load exceeds the bearing capacity, force peaks at the failure point. Stage III shows force decreasing with displacement, presenting oblique shear fracture.

The average ultimate crushing load of eight segments (14 mm diameter, 37.5 mm length) is 1451.8 N, with a corresponding ultimate displacement of 4.43 mm.

Plackett-Burman Test Significance Analysis

Design-Expert software was used to conduct ANOVA and t-tests (Table 7, Figure 6). For ultimate crushing load F_R, the influencing order was E > B > A > D > C; E, B and A posed significant effects (P<0.05) with all positive effect values, as confirmed by the Pareto chart. For ultimate crushing displacement L, the order was A > E > D > B > C; A, E and D showed significant effects (P<0.05), with positive effects for E, D, B, C and negative effect for A, as confirmed by the Pareto chart.

Table 7

Plackett-Burman test significance analysis

F_R					
Source of Variation	Sum of Squares	df	Mean Square	F-value	P-value
Model	1.302×10^5	5	26047.02	308.69	< 0.0001**
A	2552.08	1	2552.08	30.27	0.0015**
B	18802.08	1	18802.08	223.02	< 0.0001**
C	0.0833	1	0.0833	0.0010	0.9759
D	10.08	1	10.08	0.1196	0.7413
E	1.089×10^5	1	1.089×10^5	1291.38	< 0.0001**
Residual	505.83	6	84.31		
Total	1.307×10^5	11			

L					
Source of Variation	Sum of Squares	df	Mean Square	F-value	P-value
Model	1.22	5	0.2448	8.04	0.0123*
A	0.5250	1	0.5250	17.23	0.0060**
B	0.1704	1	0.1704	5.59	0.0559
C	0.0154	1	0.0154	0.5058	0.5037
D	0.1900	1	0.1900	6.24	0.0467*
E	0.3234	1	0.3234	10.62	0.0173*
Residual	0.1828	6	0.0305		
Total	1.41	11			

Note: * indicates significant difference (P<0.05), ** indicates highly significant difference (P<0.01). The same applies below.

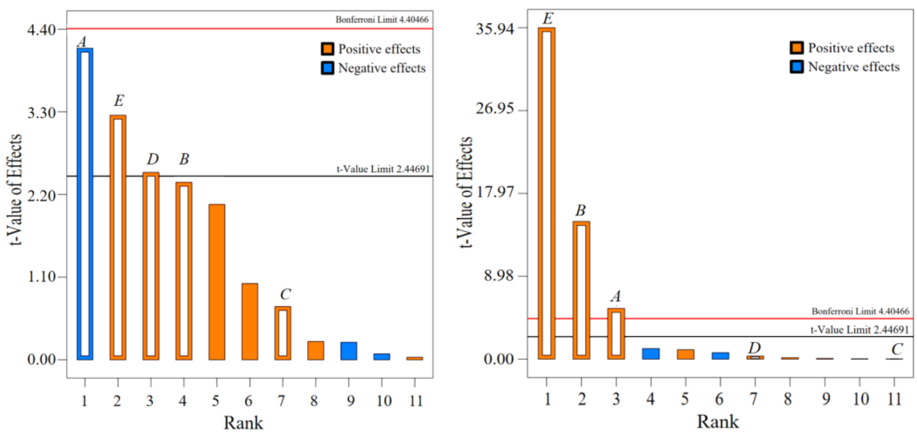

(a) Compression Displacement Pareto Chart (b) Compression Load Pareto Chart

Fig. 6 - Pareto charts

Steepest Ascent Test Analysis

Combining the data in Table 4, it can be observed that the error between the simulated ultimate crushing load/displacement and the real values first decreased and then increased during the steepest ascent experiment. The 7th test group exhibited the highest agreement between the simulated F_R and L values and the real values.

Box-Behnken Test Significance Analysis and Parameter Optimization

Design-Expert 13 software was used to analyze the experimental data in Table 6. The ANOVA results are presented in Table 8. From Table 8, it can be seen that the quadratic regression models for both F_R and L were highly significant (P < 0.0001), and the lack-of-fit terms were not significant (P > 0.05), indicating high model accuracy. Factors A, B, and E were significant for both responses. For F_R, the order of influence was E > A > B. For L, the order of influence was also E > A > B.

The regression equations relating the factors to the ultimate crushing load F_R and ultimate crushing displacement L are:

$$\begin{cases} F_R = 1458 + 36.93A + 14.67B + 0.7667D + 39.44E + 2.6AB + 0.475AD - 9.47AE \\ \quad - 2.63BD + 0.45BE + 0.25DE - 6.65A^2 + 1.92B^2 + 2.73D^2 - 4.31E^2 \\ L = 4.45 + 0.5033A + 0.1558B + 0.0317D + 0.4808E + 0.325AB + 0.005AD - 0.125AE \\ \quad - 0.035BD + 0.1625BE - 0.025DE - 0.2067A^2 - 0.018B^2 - 0.1318D^2 - 0.003E^2 \end{cases} \tag{3}$$

Table 8

Box-Behnken test significance analysis

F_R					
Source of Variation	Sum of Squares	df	Mean Square	F-value	P-value
Model	38595.97	14	2756.85	18.41	< 0.0001**
A-A	16368.85	1	16368.85	109.29	< 0.0001**
B-B	2584.27	1	2584.27	17.26	0.0010*
D-D	7.05	1	7.05	0.0471	0.8313
E-E	18667.74	1	18667.74	124.64	< 0.0001**
AB	27.04	1	27.04	0.1805	0.6774
AD	0.9025	1	0.9025	0.0060	0.9392
AE	359.10	1	359.10	2.40	0.1438
BD	27.56	1	27.56	0.1840	0.6745
BE	0.8100	1	0.8100	0.0054	0.9424
DE	0.2500	1	0.2500	0.0017	0.9680
A^2	286.49	1	286.49	1.91	0.1883
B^2	23.83	1	23.83	0.1591	0.6960
D^2	48.31	1	48.31	0.3226	0.5791
E^2	120.40	1	120.40	0.8039	0.3851
Residual	2096.76	14	149.77		
Lack of Fit	1754.76	10	175.48	2.05	0.2547
Total	40692.73	28			

L					
Source of Variation	Sum of Squares	df	Mean Square	F-value	P-value
Model	7.07	14	0.5053	17.58	< 0.0001**
A-A	3.04	1	3.04	105.78	< 0.0001**
B-B	0.2914	1	0.2914	10.14	0.0066*
D-D	0.0120	1	0.0120	0.4187	0.5281
E-E	2.77	1	2.77	96.53	< 0.0001**
AB	0.4225	1	0.4225	14.70	0.0018*
AD	0.0001	1	0.0001	0.0035	0.9538
AE	0.0625	1	0.0625	2.17	0.1624
BD	0.0049	1	0.0049	0.1705	0.6859
BE	0.1056	1	0.1056	3.68	0.0759
DE	0.0025	1	0.0025	0.0870	0.7724
A^2	0.2773	1	0.2773	9.65	0.0077*
B^2	0.0021	1	0.0021	0.0731	0.7908
D^2	0.1126	1	0.1126	3.92	0.0678
E^2	0.0001	1	0.0001	0.0020	0.9647
Residual	0.4024	14	0.0287		
Lack of Fit	0.3124	10	0.0312	1.39	0.4022
Total	7.48	28			

To precisely determine the optimal parameter combination for each factor, the constraint range needed to be further narrowed. The target values for F_R and L were known to be 1451.8 N and 4.43 mm, respectively. Combining the data from Table 6, experimental runs 2, 11, 26, and 28 exhibited F_R and L values closest to the actual values. Based on the ANOVA results, since factor D had the lowest influence on both F_R and L, it was fixed at its central level (8.55×10⁶Pa). The constraint ranges were set as follows:

$$\begin{cases} F = 1451.8\text{N} \\ L = 4.43\text{mm} \\ 4.55\times10^6\,\text{N/m}^3 \le A \le 6.25\times10^6\,\text{N/m}^3 \\ 9.15\times10^6\,\text{N/m}^3 \le B \le 9.41\times10^6\,\text{N/m}^3 \\ D = 8.55\times10^6\,Pa \\ 0.635 \le E \le 0.645 \end{cases} \tag{4}$$

Optimization solving was performed using Design-Expert 13. The optimal solution yielded values of A=5.3603×10^6 N/m³, B=9.23842×10^6 N/m³, D=8.55×10^6 Pa, E=0.635 mm. At this point, the predicted values for F_R and L were 1451.8 N and 4.38 mm, respectively. A simulation verification run using this parameter combination resulted in simulated F_R and L values of 1451.2 N and 4.31 mm, respectively. The relative errors compared to the real values were 0.04% and 1.6%, respectively.

As shown in Figure 7, the simulation results for load and displacement are generally consistent with the experimental data. The relative errors of the simulated values compared to the actual measurements are 0.04% and 1.6%, respectively. These findings suggest that the aforementioned parameters exhibit a high degree of reliability, thereby validating the applicability of the discrete element method for simulating the mechanical behavior of Astragalus roots.

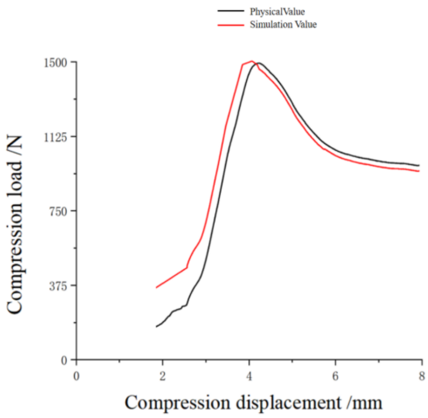

Fig. 7 - Deviation diagram of simulation value and test value

Verification test of the Bonding model breakage of Astragalus Root Granules

Experimental purpose

To verify the reliability of the parameter combination for the Astragalus root granule bonding model, this study simulated its actual crushing process in a hammer mill (including hammer impact, cavity wall extrusion and toothed ring shearing). The bond state and velocity distribution data were obtained to validate the model's characterization ability for Astragalus root crushing mechanics. The results provide theoretical support for the rotational speed optimization and structural improvement of traditional Chinese medicine hammer mills.

Test Equipment and Model Construction

Test equipment and materials

A small hammer-type pulverizer for Chinese medicinal materials (Figure 8) was used in the experiment. Its core parameters include a crushing chamber inner diameter of 165 mm and a screen mesh diameter of 0.5 mm. During operation, the high-speed rotating hammers impact and shear the material with toothed rings, and the screen controls the particle size. The experimental material was Astragalus roots from Dingxi, Gansu, cut into standard segments of 37.5 mm in length and 14 mm in diameter. Five intact and uniform segments were selected for the test.

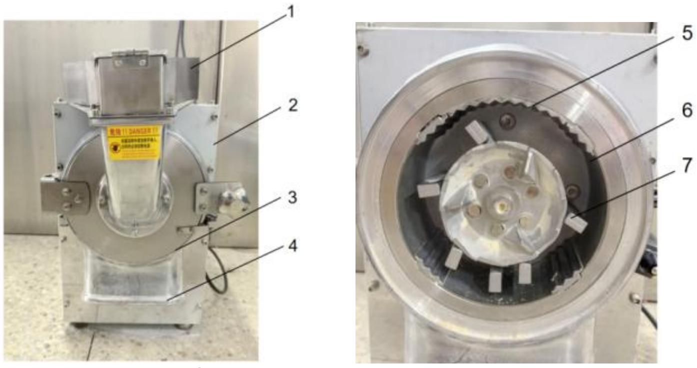

Fig. 8 - Chinese herbal medicine pulverizer

1. feed inlet; 2. electrical control box; 3. crushing chamber; 4. Discharge outlet; 5. toothed ring; 6. screen; 7. hammers

3D model and simulation Settings

The three-dimensional model of the inner wall of the crusher was constructed using SolidWorks 2024 (as shown in Figure 9a), including the crushing chamber, hammer pieces, toothed ring and other structures. The model was exported in .STL format and then imported into the Discrete element software EDEM 2022.

The virtual simulation test was conducted at the same rotor speed as the real test. The calculation formula for the particle breakage rate η of Astragalus root under each condition is:

$$\eta = \frac{m_1}{m_0} \times 100\% \tag{5}$$

In the formula:

m_1 represents the mass of the powder, (g)'

m_0-total mass of Astragalus membranaceus roots in the test, 20.5 g

A total of 7,200 1 mm-diameter Astragalus granules were bonded to construct the Astragalus root granule model using the bonding model (Figure 9b). According to the material parameters in Table 1, the Poisson's ratio, density and shear modulus of Astragalus granules and steel crushing components were defined, and the collision recovery coefficient, static and rolling friction coefficients between Astragalus and steel, as well as those between Astragalus granules were set. The crusher geometry and Astragalus root granule model were imported into the discrete element software (Figure 9c). The simulation was run for 30 s with a time step of 7.0×10^{-6} s and data saved every 0.01 s to reproduce the actual crushing process of Astragalus root.

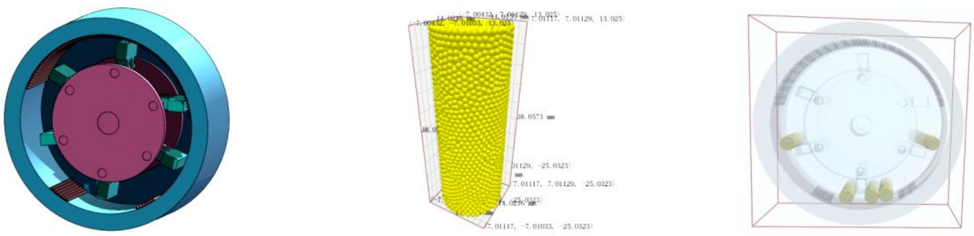

(a) Three-dimensional model of the inner wall; (b) Astragalus Root Granules Bonding model; (c) Simulation diagram

Fig. 9 - Schematic diagram of simulation modeling for crushing Astragalus root

Test method

Real crushing experiment

A real crushing test of Astragalus roots was conducted using the traditional Chinese medicine hammer crusher shown in Figure 10. Before the test, the equipment was pre-started, and Astragalus roots were fed slowly after the rotor speed stabilized. In the crushing chamber, roots were crushed by hammer impact, chamber wall compression and inter-particle collision, with crushed products discharged from the lower outlet. During the test, samples from the outlet and chamber inner wall were collected every 5 seconds. Morphology photos were taken at 5, 10, 15, 20, 25 and 30 seconds (right side of Figure 10), and the test was terminated at 30 seconds.

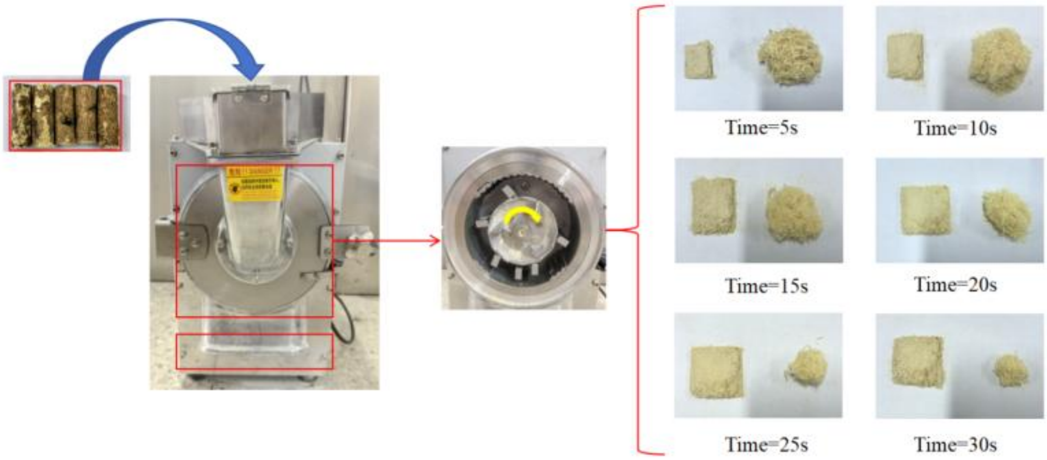

Fig. 10 - Bench test

Simulation crushing test

In EDEM 2022, rotor speed was set to 2840 r/min to match physical conditions. The discrete element model of Astragalus root particles, constructed based on the Bonding model, was imported to simulate the crushing process. Velocity field, vector distribution, and bond status evolution were recorded at 0, 5, 10, 15, 20, 25, and 30 s, with results shown in Figure 11.

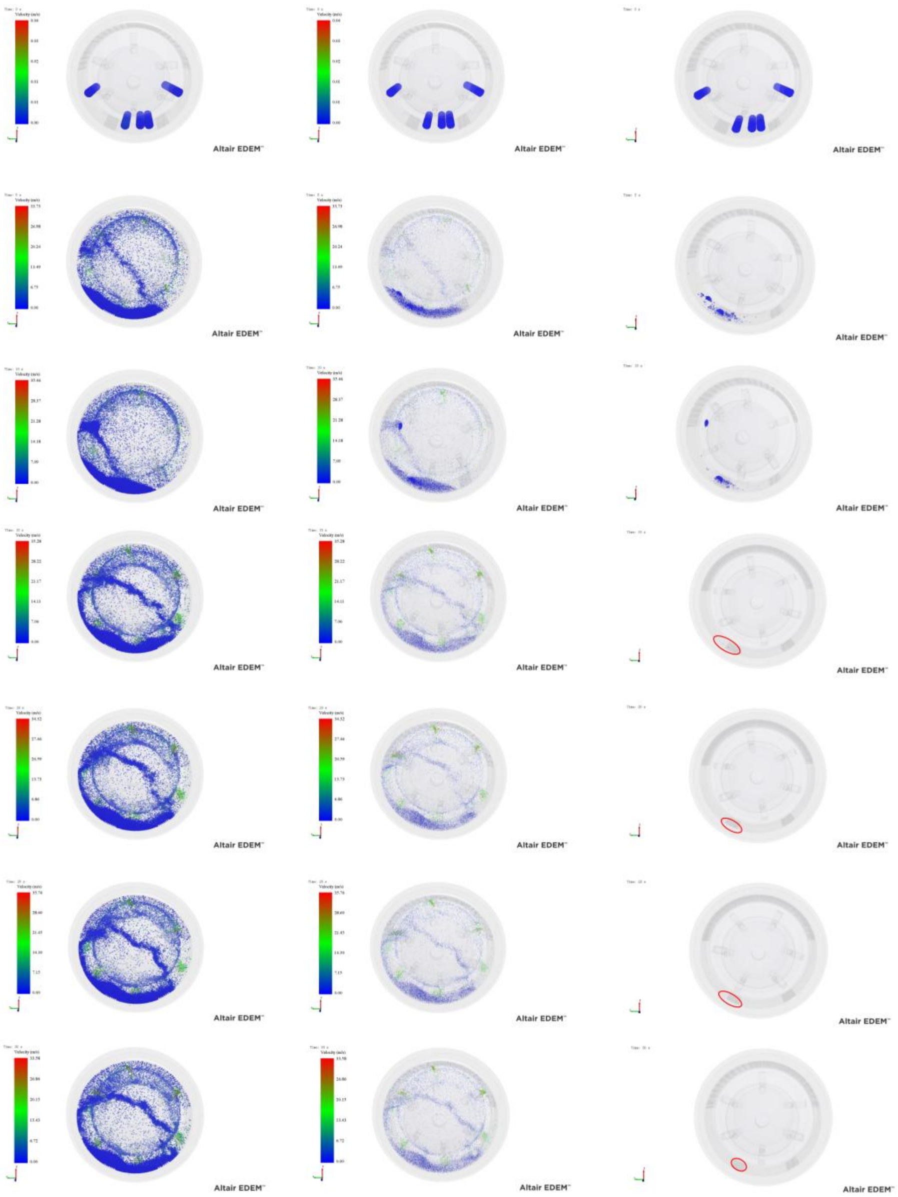

Fig. 11 - Simulation process of crushing Astragalus Root Granules

Test results

At a crusher speed of 2840 r/min, the error between the simulated and actual crushing rates of Astragalus root granules is 6.3%–12.7% as shown in Figure 12, which verifies the high accuracy of the calibrated bonding model parameters.

The crushing simulation presents three successive stages: initially, particles are agglomerated and static with complete bonds; subsequently, particles disperse and refine with increased velocity differences and large-scale bond breakage; finally, particles become fine and uniform, accompanied by a stable velocity field and nearly full bond dissociation.

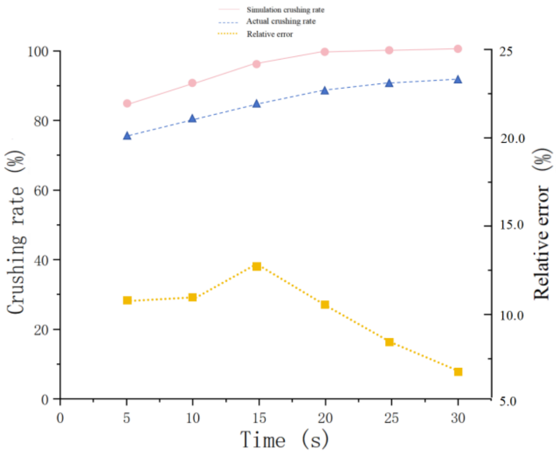

Fig. 12 - The breakage rate at different times

CONCLUSIONS

Uniaxial compression tests of Astragalus root segments were carried out to obtain its mechanical properties, with an ultimate crushing load of 1451.8 N and an ultimate crushing displacement of 4.43 mm. Significant factors were screened via the Plackett-Burman design, the parameter range was narrowed by the steepest ascent test, and the optimal Bonding Model parameters were determined by Box-Behnken optimization: normal stiffness per unit area 5.3603×10^6 N/m³, shear stiffness per unit area 9.23842×10^6 N/m³, critical shear stress 8.55×10^6Pa, bonded disk radius 0.635 mm. Uniaxial compression simulation verification shows that the relative errors of ultimate crushing load and displacement are only 0.04% and 1.6%, respectively. The parameters were applied to Astragalus root crushing simulation, accurately characterizing the evolution of velocity field, vector distribution and bond state, with a crushing rate error of 6.3%–12.7%, verifying their reliability. This study provides accurate parameter support for DEM simulation and intelligent design of Astragalus processing equipment, and offers a new reference for mechanical simulation of granular Chinese medicinal materials.

ACKNOWLEDGEMENT

This study was supported by Natural Science Foundation of Jiangsu Province, China (BK20241058).

REFERENCES

[1] Cundall, P.A., Strack, O.D.L. (1979). A Discrete Numerical Model for Granular Assemblies. *Géotechnique*, 29(1), 47–65. https://doi.org/10.1680/geot.1979.29.1.47.

[2] Duan, Q.M. (2005). *Study on Biological Characteristics of Astragalus membranaceus*. [Master's Thesis], Northwest A&F University, Yangling, China.

[3] Du, X., Liu, C.L., Jiang, M., Yuan, H., Dai, L., Li, F.L. (2022). Calibration of Bonding Model Parameters for Coated Fertilizers Based on Discrete Element Method. *Transactions of the Chinese Society for Agricultural Machinery*, 53, 141-149. http://doi.org/10.6041/j.issn.1000-1298.2022.07.014.

[4] Gao, Q., Cheng, L., Wang, R., Chen, M., Zhao, W., Fu, J., Wang, Z. (2024). Discrete Element Model Building and Optimization of Tomato Stalks at Harvest. *Agriculture*, 14, 531. http://doi.org/10.3390/agriculture14040531.

[5] Hu, M., Xia, J., Zhou, Y., Luo, C., Zhou, M., Liu, Z. (2022). Measurement and Calibration of the Discrete Element Parameters of Coated Delinted Cotton Seeds. *Agriculture*, 12, 286. http://doi.org/10.3390/agriculture12020286.

[6] Ji, X.M., Wang, W.Q., Liu, L. (1998). Brief Summary on Efficacy Research of Astragalus membranaceus. *Journal of Shandong University of Traditional Chinese Medicine*, 22(3), 65-67. https://doi.org/10.16294/j.cnki.1007-659x.1998.03.030.

[7] Li, C., Liu, Z., Geng, L., Xu, T., Feng, W., Liu, M., Qiao, D., Wang, Y., Wang, J. (2025). The Establishment of a High-Moisture Corn Ear Model Based on the Discrete Element Method and the Calibration of Bonding Parameters. *Agriculture*, 15, 752. http://doi.org/10.3390/agriculture15070752.

[8] Li, H., Meng, Y.B., Qi, X.D, Wang, Y.J., Li, Y.Q., Li, M.Y. (2025). Discrete Element Modeling Method and Parameter Calibration for Garlic Cloves Based on Bonding V2 Model. *Transactions of the Chinese Society for Agricultural Machinery*, 54, 1-11. http://doi.org/10.6041/j.issn.1000-1298.2025.07.013.

[9] Lu, G., Third, J.R., Müller, C.R. (2015). Discrete Element Models for Non-Spherical Particle Systems: From Theoretical Developments to Applications. *Chemical Engineering Science*, 127, 425-465. http://dx.doi.org/10.1016/j.ces.2014.11.050.

[10] Mu, X., Li, H., Wang, Z., Wang, Q., Geng, D., Zhu, J. (2023). Comparison of Crushing Effect of Differently Shaped Crushing Rollers on Whole-Plant Silage Maize. *Agriculture*, 13, 1276. http://doi.org/10.3390/agriculture13071276.

[11] Potyondy, D.O., Cundall, P.A. (2004). A Bonded-Particle Model for Rock. *International Journal of Rock Mechanics and Mining Sciences*, 41, 1329-1364. http://doi.org/10.1016/j.ijrmms.2004.09.011.

[12] Shen, Z., Jiang, M., Thornton, C. (2016). DEM Simulation of Bonded Granular Material. Part I: Contact Model and Application to Cemented Sand. *Computers and Geotechnics*, 75, 192-209. http://dx.doi.org/10.1016/j.compgeo.2016.02.007.

[13] Su, Y., Xu, Y., Cui, T., Gao, X., Xia, G., Li, Y., Qiao, M. (2021). Determination and Interpretation of Bonded-Particle Model Parameters for Simulation of Maize Kernels. *Biosystems Engineering*, 210, 193-205. http://doi.org/10.1016/j.biosystemseng.2021.08.022.

[14] Xi, J.Y., Su, Y.J., Zhao, K.P., Feng, J.L., Yang, F.D. (2023). Research Progress on the Dual-Use of Astragalus as Medicine and Food. *West China Journal of Pharmaceutical Sciences*, 38, 718-724. http://doi.org/10.13375/j.cnki.wcjps.2023.06.023.

[15] Xie, W., Peng, L., Jiang, P., Meng, D., Wang, X. (2023). Establishment and Optimization of Dual-Layer Bonding Discrete Element Model for Oilseed Rape Stem at Harvest. *Transactions of the Chinese Society for Agricultural Machinery*, 54, 112-120. http://doi.org/10.6041/j.issn.1000-1298.2023.05.011.

[16] Xu, J., Sun, S., Li, X., Zeng, Z., Han, C., Tang, T., Wu, W. (2024). Research on the Population Flow and Mixing Characteristics of Pelleted Vegetable Seeds Based on the Bonded-Particle Model. *Agriculture*, 14, 752. http://doi.org/10.3390/agriculture14050752.

[17] Zeng, Z.W., Ma, X., Cao, X.L., Li, Z.H., Wang, X.C. (2021). Critical Review of Applications of Discrete Element Method in Agricultural Engineering. *Transactions of the Chinese Society for Agricultural Machinery*, 52, 1-20. http://doi.org/10.6041/j.issn.1000-1298.2021.04.001.

[18] Zhang, H., Wen, Z., Chen, Y., Liu, J., Liu, H., Zhang, Z., Zhang, X. (2023). Research on Cutting Angle Design Optimization of Rubber Cutter Based on Discrete Element Method. *Agriculture*, 13, 1894. http://doi.org/10.3390/agriculture13101894.

[19] Zhang, X., Hu, X., Liu, J., Yang, Y., Li, Y. (2023). Discrete Element Simulation Bonding Model Parameter Calibration and Testing of Banana Stems. *Transactions of the Chinese Society for Agricultural Machinery*, 54, 121-130. http://doi.org/10.6041/j.issn.1000-1298.2023.05.012.

[20] Zhao, H., Huang, Y., Liu, Z., Liu, W., Zheng, Z. (2021). Applications of Discrete Element Method in the Research of Agricultural Machinery: A Review. *Agriculture,* 11, 425. http://doi.org/10.3390/agriculture11050425.

[21] Zhong, G., Li, H., He, J., Wang, Q., Lu, C., Wang, C., Tong, Z., Cui, D., He, D. (2023). Design and Test of Single-Disc Opener for No-Till Planter Based on Support Cutting. *Agriculture*, 13, 1635. http://doi.org/10.3390/agriculture13081635.

[22] Zhou, B., Zuo, Y., Hou, L. (2023). Parameter Calibration of Xinjiang Paperbark Walnut Kernels by Discrete Element Simulation. *Agriculture*, 13, 353. http://doi.org/10.3390/agriculture13020353.

[23] Zhu, H., He, X., Shang, S., Zhao, Z., Wang, H., Tan, Y., Li, C., Wang, D. (2022). Evaluation of Soil-Cutting and Plant-Crushing Performance of Rotary Blades with Double-Eccentric Circular-Edge Curve for Harvesting Cyperus esculentus. *Agriculture*, 12, 862. http://doi.org/10.3390/agriculture12060862.